Received: 15 December 2020 | Revised: 18 June 2021 | Accepted: 31 August 2021

DOI: 10.1002/we.2688

RESEARCH ARTICLE

WILEY

Numerical investigation of wind turbine wakes under high thrust coefficient

Luis A Martínez-Tossas[1] | Emmanuel Branlard[1] | Kelsey Shaler[1] | Ganesh Vijayakumar[1] | Shreyas Ananthan[2] | Philip Sakievich[3] | Jason Jonkman[1]

[1]National Renewable Energy Laboratory, Golden, Colorado, USA

[2]Siemens Gamesa Renewable Energy Inc., Boulder, Colorado, USA

[3]Sandia National Laboratories, Albuquerque, New Mexico, USA

Correspondence
Luis A Martínez-Tossas, National Renewable Energy Laboratory, Golden, CO, USA.
Email: Luis.martinez@nrel.gov

Funding information
National Nuclear Security Administration, Grant/Award Number: DE-NA0003525; Wind Energy Technologies Office, Grant/Award Number: DE-AC36-08GO28308

Abstract

We study wind turbine wakes of rotors operating at high thrust coefficients (C_T > 24/25) using large-eddy simulations with a rotating actuator disk model. Wind turbine wakes at high thrust coefficients are different from wakes at low thrust coefficients. Wakes behave differently at high thrust, with increased turbulence and faster recovery. Lower induction in the wake is achieved because wakes in high-thrust conditions recover much faster than in normal operating conditions. This enhanced recovery is possible thanks to the turbulence generated in the near wake. We explore the mechanism behind this behavior and propose a simple model to reproduce it. We also propose a Gaussian fit for the wakes under high-thrust conditions and use it use it to initialize an Ainslie type model within the FAST.Farm framework.

KEYWORDS
FAST.Farm, high thrust coefficient, large-eddy simulations, wake

1 | INTRODUCTION

Wind turbine wakes are typically characterized in terms of the thrust coefficient. The thrust coefficient is a nondimensional number that compares the axial force exerted on the flow by the turbine to the incoming momentum of the flow. The thrust coefficient is defined as

$$C_T = \frac{T}{\frac{1}{2}\rho A U_\infty^2} \tag{1}$$

where T is the thrust force (streamwise direction) from the turbine, ρ is the fluid density, A is the rotor swept area, and U_∞ is the upstream inflow velocity. In this work, we use large-eddy simulations (LES) to study wind turbine wakes with high thrust coefficients of C_T > 24/25. We define the high-thrust limit as C_T > 24/25 based on the work of Moriarty et al.[1] This limit is based on the momentum balance when the axial induction is $a = 0.4$.[1] Around this value, the standard relation between thrust and induction changes from a momentum balance to an empirical approximation.[1] Wind turbines often operate in high-thrust conditions when operating at low wind speeds—in control region 1.5—where the rotor speed and tip-speed ratio tend to be higher than optimal to minimize the rotor-speed range and avoid tower resonance. In standard soft-stiff tower designs, control region 1.5 is introduced, which sets a lower limit on how low the variable rotor speed can go.[2] So, often at wind speeds below 7–8 m/s, the wind turbine operates at a tip-speed ratio that is higher than optimal, which results in C_T values at these wind speeds higher than 24/25.

The motivation of this work is to improve our understanding of wind turbine wakes in high-thrust conditions to develop better engineering wake models.[3,4] Wind turbines often operate in high-thrust conditions at low wind speeds (control region 1.5) for typical soft-stiff tower designs, where the tower-bending natural frequency is placed between the once- and thrice-per-revolution frequencies. In this case, the rotor typically spins at a speed higher than optimal for power capture at low wind speeds to avoid resonance of the tower-bending natural frequency. Wake models typically rely on the thrust coefficient as an input to compute the velocity deficit of the wake. In the case of thrust coefficients below $C_T \approx 24/25$, the axial momentum theory is a good approximation relating the thrust coefficient, velocity at the rotor, and velocity in the far wake. However, when the thrust coefficient is greater than $C_T = 24/25$, the relation between axial induction and thrust coefficient changes, along with the mechanism behind the formation and development of the wake. We study this mechanism using LES and compare the wakes of wind turbines for different thrust coefficients.

Axial induction is used to describe the velocity at the rotor plane as a fraction of the inflow velocity, $a = 1 - \frac{u_d}{U_\infty}$, where u_d is the disk-averaged velocity and U_∞ is the time-averaged inflow velocity. Figure 1 compares the thrust coefficients to axial induction, showing the standard curve from the literature and experimental measurements.[5] There are different wake states that create a different relation between the thrust coefficient and the induction at the rotor plane. In the windmill state described by axial momentum theory, the induction at the rotor plane is half of the induction in the fully developed wake. In this case, the velocity in the fully developed wake becomes $u_w = U_\infty(1-2a)$. This leads to good agreement between simulations and experimental data in the case of low thrust and low induction. The data points for cases with high thrust coefficients are scattered and do not follow a straight line. In the turbulent and vortex ring wake states ($C_T \geq 24/25$ and induction $a \geq 0.4$), the relationship between the induction at the rotor plane and the far wake changes. This relationship is not well understood in terms of simple axial momentum theory, and empirical formulas are used to relate the induction at the rotor plane with the thrust coefficient, for example, the Glauert correction.[6,7] Figure 2 shows a cut plane of time-averaged velocity magnitude and streamlines

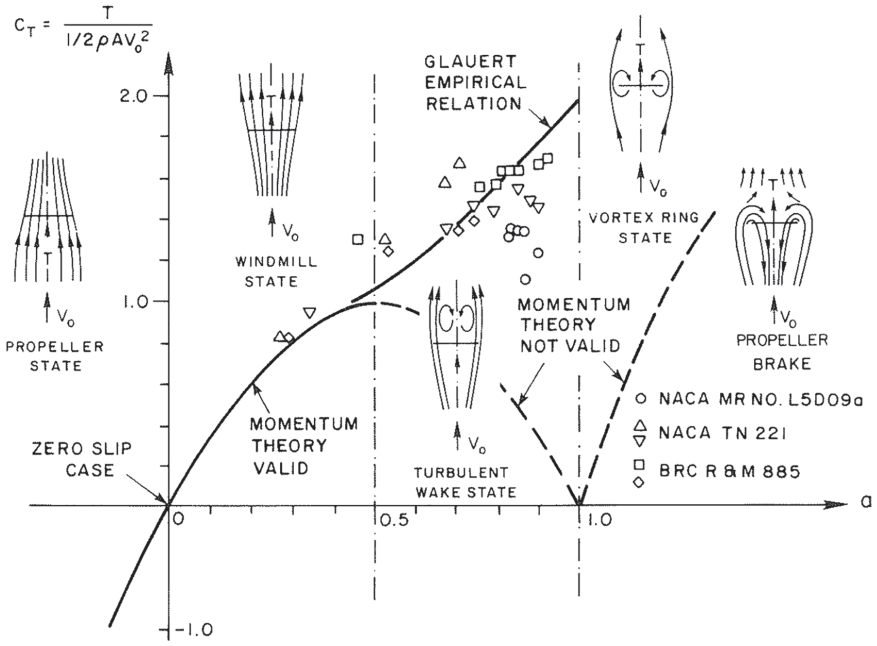

FIGURE 1 Thrust coefficient (C_T) as a function of average induction at the rotor plane (a). Figure from Eggleston and Stoddard[5]

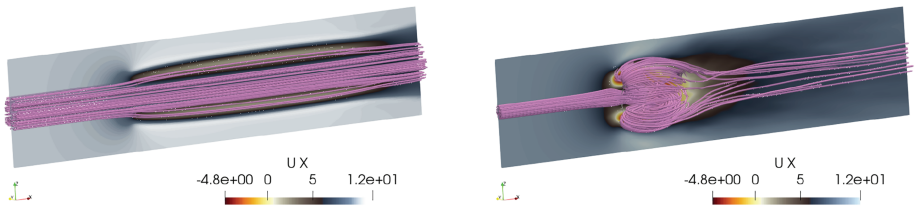

FIGURE 2 Mean velocity across the wake and streamlines for simulations with $C_T = 0.5$ (left) and $C_T = 1.5$ (right)

from LES with $C_T = 0.5$ and $C_T = 1.5$. We see that streamlines for a high thrust coefficient ($C_T = 1.5$) are very different from the standard case ($C_T = 0.5$). The mechanism of wake formation and evolution in the case of high thrust coefficients is different from the case of lower thrust coefficients. In the high-thrust case, the streamlines expand as they pass through the rotor. After passing through the rotor plane, they move closer to the center of the wake.

There are two main ways to change the thrust coefficient of a wind turbine at a given wind speed. The first one is by changing the pitch angle of the blade, and the second one is by changing the rotational speed, which changes the tip speed ratio. It is also possible to change both pitch and rotational speed to achieve different thrust coefficients. In this work, we use LES of an actuator disk model to represent a wind turbine under uniform inflow. Simulations are performed with different thrust coefficients, as well as different radial force distributions with similar thrust coefficients. The latter cases are important because different force distributions result in different near-wake development. LES is used, as opposed to a time-averaged formulation such as Reynolds-averaged Navier–Stokes (RANS), to capture the turbulent and dynamic nature of the wake that results from high thrust coefficient turbine operation.

We develop an understanding of the mechanism in the formation of a high-thrust wake by using a simplified model that studies the evolution of a streamtube that passes through the disk. Then, we use the results obtained from LES to improve the near-wake model used in FAST.Farm. FAST.Farm is a midfidelity tool used to predict time-dependent wind farm flows based on advancements to the dynamic wake meandering model.[8,9] In FAST.Farm, wakes are generated and advected using the velocity from the ambient inflow (either an LES precursor or a synthetic turbulence) and wake induced velocity and—before this work—the velocity in the wake was based on momentum theory and only valid for low-thrust conditions.

2 | METHODOLOGY

We perform LES using an actuator disk model within the ExaWind framework.[10] The simulations are performed using Nalu-Wind, an incompressible LES solver. Nalu-Wind is a derivative of Nalu, a low-mach number computational fluid dynamics (CFD) code, which uses an unstructured finite-volume formulation with primitive variables. The numerics of Nalu have been verified in the literature using different applications.[11-14] Nalu-Wind uses most of the features and numerics from Nalu with an added collection of wind energy features, including actuator disks/lines, atmospheric boundary layers, and blade-resolved wind turbine simulations. Nalu-Wind is being verified and validated following the road map from the US Department of Energy.[15] As part of the verification and validation road map, Nalu-Wind has been compared with other codes and field experiments in recent work.[16,17] The turbine is modeled using an actuator disk model coupled with OpenFAST to compute aerodynamic forces and rotational effects. Nalu-Wind's actuator disk model is somewhat unique because it takes an underlying OpenFAST actuator line model and expands the discretization into the azimuthal direction for spreading forces in the LES domain.[18,19] The procedure for coupling the actuator disk and line models in the respective LES and OpenFAST domains is as follows. First, the velocity in the LES domain is sampled with the actuator line points. Next, the OpenFAST actuator line model is sub-cycled in time to compute the aerodynamic forces. The forces from the OpenFAST actuator line blades are then azimuthally averaged and applied to all the points in the disk's azimuthal discretization. Finally, the forces at the actuator disk discretization points are spread back to the LES domain through a standard Gaussian kernel with $\epsilon/\Delta = 2.5$ where Δ is the grid size.[20–22] Rotational effects in the forcing are captured through temporal subcycling of the OpenFAST model in between LES timesteps. Azimuthal averaging in the fluid LES domain's actuator disk model washes out some of these effects in the LES domain (i.e., tower shadowing, and tip vortices) because it acts as a time average for the rotation of the blades. However, this allows the disk to be insensitive to the fluid domain's timestep and thus offers a significant computational advantage over using an actuator line model in the LES domain. The computational domain is a box of 20D by 20D by 20D where D is the rotor diameter and the turbine is in the center of the domain. There is local refinement near the turbine with 40 grid points across the diameter and in the near-wake. Figure 3 shows a schematic of the mesh with the refinement regions used to capture the dynamics of the near-wake. The subgrid-scale stresses are modeled using the Smagorinsky model with a coefficient of $C_S = 0.08$.[23,24] The inflow velocity is 10-m/s uniform inflow and a zero gradient boundary condition is used on the sides for velocity and pressure.

The actuator disk model applies azimuthally uniform force distributions in the normal and tangential directions. Only aerodynamic forces on the blades are used and no structural displacements or tower forces are used in the model. The different radial force distributions are achieved by (1) varying pitch (Pitch), (2) varying rotational speed (revolutions per minute, RPM), and (3) prescribing a constant loading along the blade (Constant C_t). In the cases of Pitch and RPM, the forces for the actuator disk are derived from the NREL 5-MW rotor.[25] The constant loading case is constant from 60% of the blade span to the tip and drops linearly to 0 loading at the root. This was done to represent turbine wake in a more realistic way and to avoid numerical instabilities associated with high loading near the hub. For every turbine operating condition, we performed simulations at 19 different thrust coefficients ranging from $C_T = 0.1$ to $C_T = 1.9$, for a total of 57 LES cases. Table 1 shows the rotational speed and blade pitch angle values for the RPM and Pitch cases. The cases with Constant C_T do not use the rotational speed nor the pitch angle as inputs.

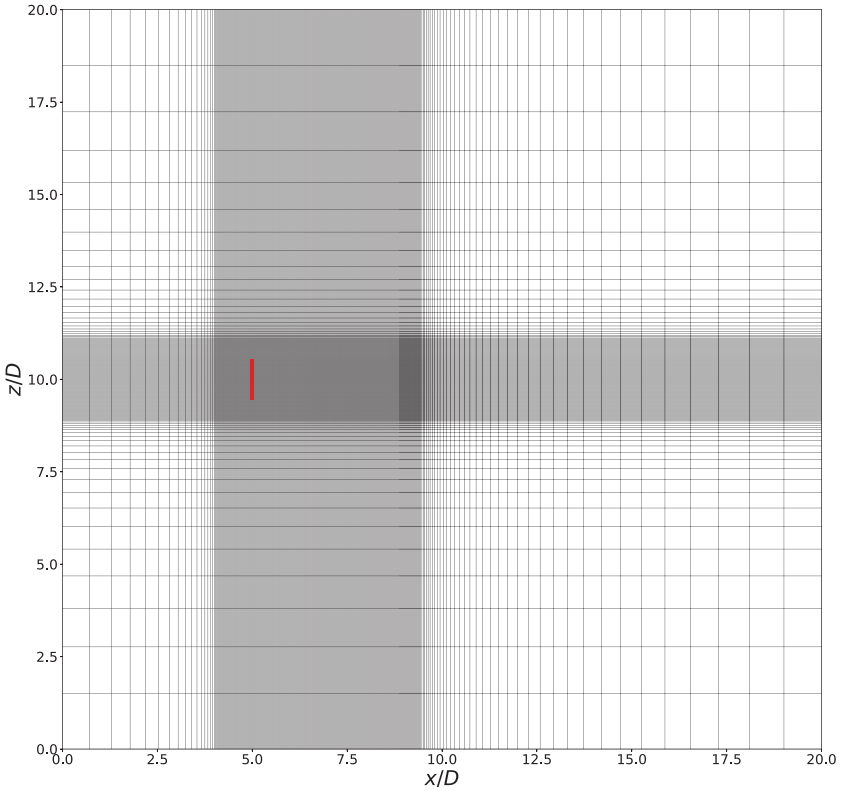

FIGURE 3 A schematic showing the extent of the domain and the refinement level used to capture the near-wake dynamics. The red line denotes the rotor location

TABLE 1 Rotational speed of the rotor and blade pitch angle for the Pitch and RPM cases

RPM Cases				Pitch Cases			
Nominal C_T	RPM	Pitch (°)	Simulation C_T	Nominal C_T	RPM	Pitch (°)	Simulation C_T
0.1	2.0	0	0.09	0.1	14.8	5.8	0.13
0.2	4.0	0	0.18	0.2	14.8	5.4	0.23
0.3	5.3	0	0.28	0.3	14.8	4.9	0.33
0.4	6.5	0	0.37	0.4	14.8	4.4	0.43
0.5	7.4	0	0.46	0.5	14.8	3.9	0.53
0.6	8.4	0	0.57	0.6	14.8	3.4	0.63
0.7	9.8	0	0.69	0.7	14.8	2.8	0.73
0.8	11.7	0	0.81	0.8	14.8	2.2	0.81
0.9	14.4	0	0.91	0.9	14.8	1.5	0.91
1.0	17.8	0	0.99	1.0	14.8	0.8	0.99
1.1	21.4	0	1.05	1.1	14.8	0.2	1.05
1.2	26.8	0	1.15	1.2	14.8	−0.4	1.11
1.3	39.5	0	1.38	1.3	14.8	−1.1	1.20
1.4	42.6	0	1.40	1.4	14.8	−2.4	1.37
1.5	45.3	0	1.41	1.5	14.8	−3.4	1.52
1.6	47.5	0	1.49	1.6	14.8	−4.0	1.60
1.7	49.6	0	1.54	1.7	14.8	−4.9	1.77
1.8	53.4	0	1.48	1.8	14.8	−5.3	1.82
1.9	55.4	0	1.50	1.9	14.8	−5.8	1.84

3 | RESULTS

We first look at the relation between rotor-averaged thrust coefficient and axial induction across the simulations and compare it to theoretical predictions. Figure 4 shows thrust coefficient as a function of axial induction at the rotor plane for all simulations, as well as axial momentum theory, $C_T = 4a(1-a)$. The formulas from Glauert, Madsen, and Buhl are shown as a reference.[6,7,26] The different symbols in Figure 4 correspond to different radial distribution of forces along the disk (Pitch, RPM and Constant C_t). The simulations predict a thrust force that is close to the expected value but not exactly the same because the operating conditions were determined using BEM. In the cases of low thrust coefficients ($C_T < 24/25$ and $a < 0.4$), all simulation points collapse and follow the theoretical line closely. In the case of high thrust coefficient, the average induction differs from the empirical model and depends on the force distribution. In these cases, the thrust coefficient changes as a function of time and the vertical lines denote the standard deviation. Similar to the data scatter in Figure 1, the different simulations do not follow the same line and the standard deviations show the variability in thrust coefficient as a function of time. This result is consistent with the results found in the literature.[7,27]

The axial momentum theory defines axial power coefficient as a function of thrust and axial induction as shown in Equation (2).

$$C_P = C_T(1-a) \tag{2}$$

Figure 5 shows the power coefficient defined in Equation (2) as a function of axial induction for all cases. There is good agreement between the theory and the simulations for low induction. All the simulation points for axial induction below $a = 0.4$ follow the theoretical line. However, discrepancies are observed for the cases of higher induction, similar to the thrust and axial induction relation from Figure 4. The disagreement at higher inductions is expected because the assumptions from the momentum theory are no longer valid for higher inductions.

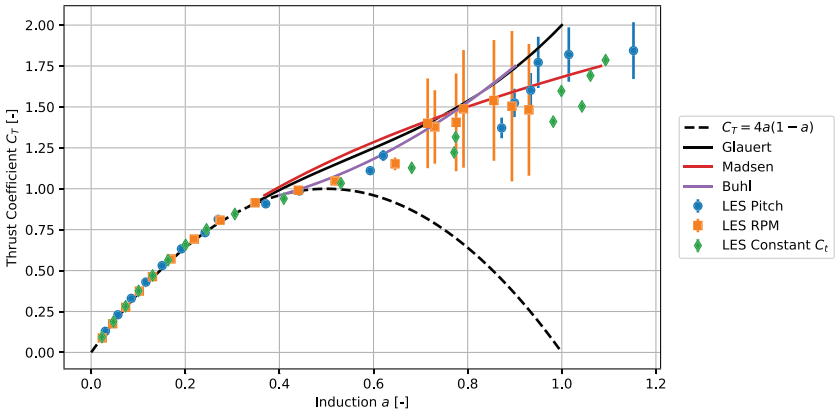

FIGURE 4 Thrust coefficient as function of average induction at the rotor plane from large-eddy simulations (LES). The vertical lines show the standard deviation of the thrust coefficient in the simulation

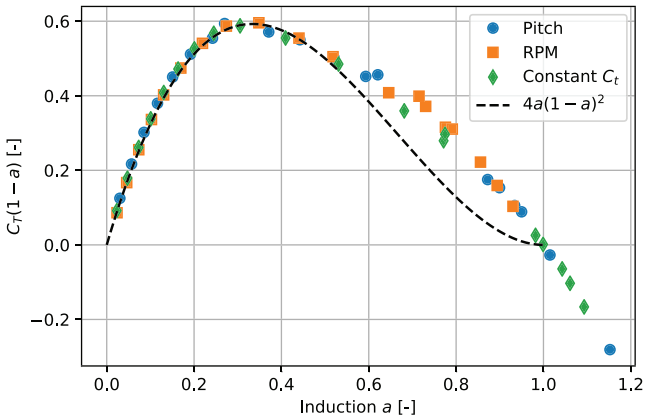

FIGURE 5 Axial power coefficient as function of average induction at the rotor plane from large-eddy simulations (LES)

3.1 | Turbine loading

We now focus on the blade load distribution for different cases. To have the same thrust coefficient and different axial inductions, different loading must be specified along the blade. Figure 6 shows axial velocity and axial force along the radial direction for thrust coefficients of $C_T \approx 0.7$ and $C_T \approx 1.3$. These two conditions are representative of the low and high thrust regions of turbine operation. We can see in Figure 6 that, even with the similar total thrust coefficient, the loading along the blade is different for the three cases. The forces along the blade have jumps because of discrete changes between different lookup tables, however the forces applied to the CFD solver are smoothed by means of the Gaussian kernel. In cases with a typical thrust coefficients ($C_T \approx 0.7$), the differences between quantities along the blade are small. However, in the case of higher thrust coefficient ($C_T \approx 1.3$), the differences are larger, causing low axial velocities (and negative in the RPM case) in parts of the blade. These differences generate an unstable wake that becomes turbulent at the rotor plane. A turbulent wake leads to much faster wake recovery, as we will see in the next section. We note that the RPM cases generate the largest difference of loading throughout the blade. This difference comes from the higher relative velocities from increasing the rotational speed.

3.2 | Wake contours

We now focus on the wake profiles for representative cases with $C_T = 0.7$ (design conditions), 1.0 (high), and 1.3 (very high). The loading along the blades is responsible for generating the velocity field at the rotor plane, which evolves and propagates downstream as the wake.

Figure 7 shows time-averaged streamwise velocity contours with streamlines for different thrust coefficients. The streamlines are time-averaged so the results can be interpreted in a time-averaged sense, especially for the highly-turbulent high-thrust cases. We want to draw attention to the time-averaged streamlines observed in the flow. The streamlines for the case of a $C_T = 0.7$ behave as expected; they expand as they pass the rotor and remain parallel further downstream. The streamlines for higher thrust coefficient ($C_T = 1.0$ and 1.3) expand as they reach the rotor and contract further downstream. This unique behavior differs from the classical understanding of wind turbine wakes for low thrust coefficients, where the streamlines expand throughout the wake until local pressure recovers to freestream pressure. It is also interesting to see that the wakes differ from each other depending on the radial distribution of forces (Ct, RPM, Pitch). However, the mechanism of the streamlines expanding and quickly contracting is present in all cases with high thrust coefficients.

Figure 8 shows instantaneous streamwise velocity fields for the different cases with $C_T = 0.7$, 1.0, and 1.3. One interesting characteristic of high thrust coefficient wakes is that they are turbulent close to the rotor. We can see the streamwise component of the resolved Reynolds stress tensor ($\overline{u'u'}/U_\infty^2$) in Figure 9. It is clear how the cases for lower thrust coefficient have a nonturbulent wake and start transitioning when the thrust coefficient is close to $C_T = 1$. In the case of higher thrust coefficient ($C_T = 1.3$), the wakes become very turbulent and increased levels of turbulence are observed in the near wake. This turbulence helps in the recovery mechanism discussed in section 4.

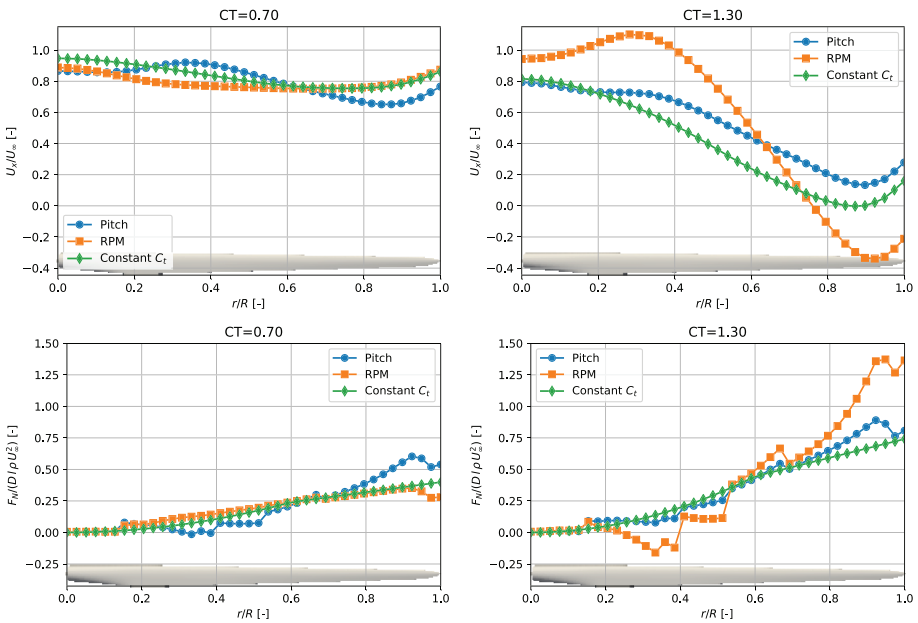

FIGURE 6 Axial force and velocity along the blade for simulations with $C_T \approx 0.7$ (left) and $C_T \approx 1.3$ (right)

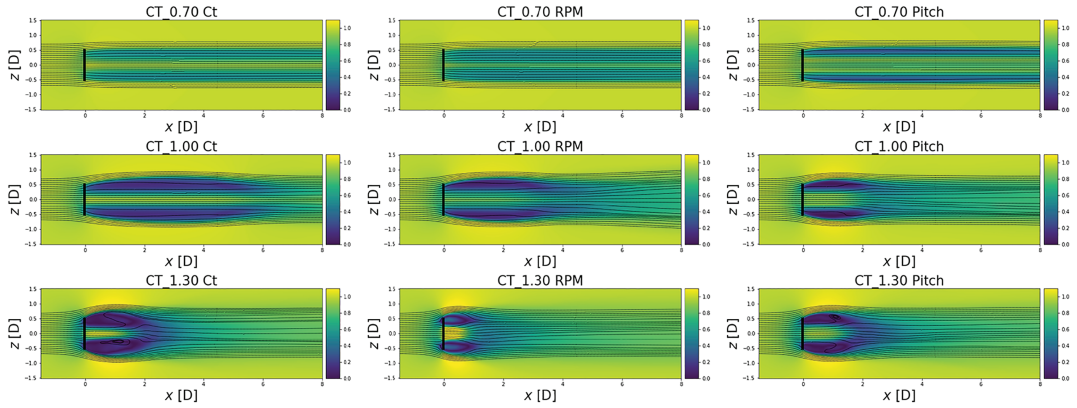

FIGURE 7 Time-averaged streamwise velocity contours with streamlines for revolutions per minute (RPM), Pitch and Constant C_t simulations with $C_T = 0.7$, 1.0, and 1.3. The rotor disk is located at $x = 0$ and marked with a line

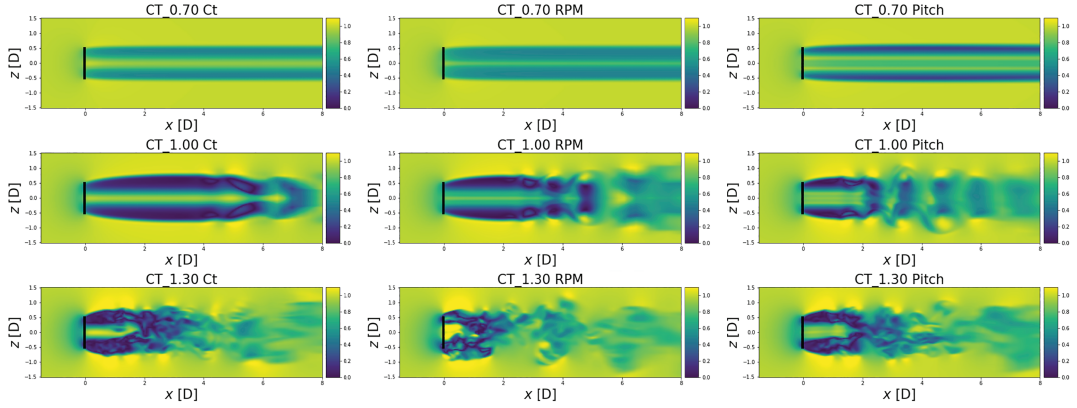

FIGURE 8 Snapshot of streamwise velocity for revolutions per minute (RPM), Pitch and Constant C_t simulations with $C_T = 0.7$, 1.0, and 1.3

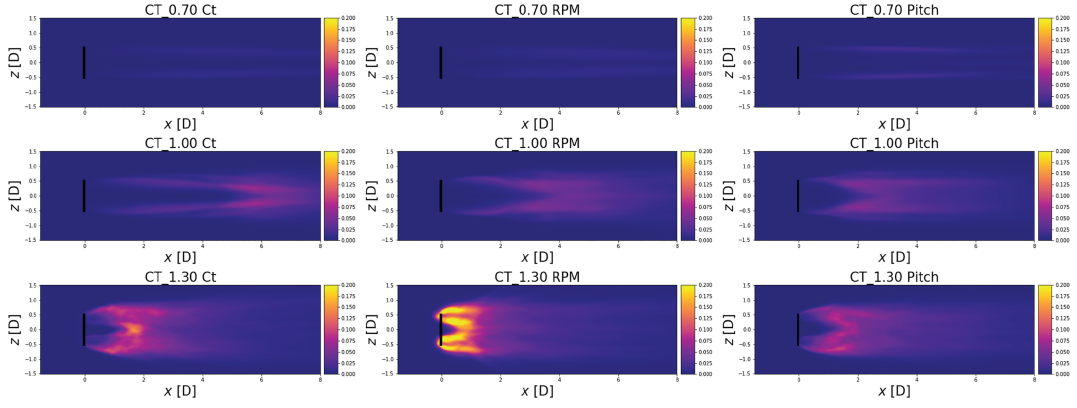

FIGURE 9 Nondimensional streamwise component of the Reynolds stress tensor $\overline{u'u'}/U_\infty^2$ for revolutions per minute (RPM), Pitch and Constant C_t cases with thrust coefficients $C_T = 0.7$, 1.0, and 1.3

The left plot in Figure 10 shows the average pressure as a function of downstream distance for cases with different thrust coefficients achieved by changing the rotational speed of the turbine. The cases with lower thrust coefficient behave as expected by having a pressure drop near the rotor and then the pressure recovers downstream. The cases with higher thrust coefficients ($C_T > = 0.9$) have a much stronger pressure drop just behind the rotor. This higher pressure drop is related to the higher thrust coefficient and allows for more turbulence and a faster wake recovery. The right plot in Figure 10 shows the average induction as a function of downstream distance. We note that the spatial averaging is

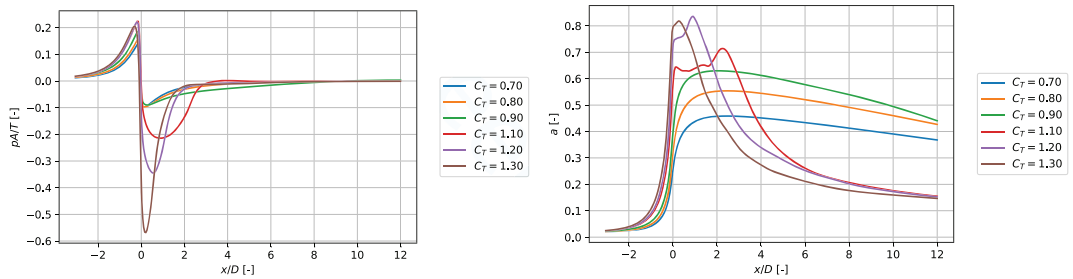

FIGURE 10 Time-averaged pressure and axial induction from large-eddy simulations (LES) spatially averaged inside the rotor circumference as a function of downstream distance

done in an area corresponding to the rotor. The inductions in the cases of lower thrust coefficients behaves as expected, increasing with downstream distance until about 2D downstream, where the induction is about twice what it is at the rotor disk. We note that the decrease in average induction is from the wake expansion. In the case of high thrust, the induction increases to very high values ($a \geq 0.5$) and decays quickly. This enhanced recovery is achieved by the higher levels of turbulence.

4 | MECHANISM IN THE WAKE OF A HIGH-THRUST WIND TURBINE

We now propose an explanation for the mechanism in the wake formation of a high-thrust wind turbine wake. The vorticity shed into the wake is directly related to the gradient of the circulation along the blade. For high-thrust conditions, the gradients of circulation throughout the blade and especially near the tip are high, leading to strong circulation values for the shed vorticity. The velocity induced by the vorticity is on the same order as the inflow velocity which leads to negative velocities in the wake. This leads to the turbulent wake state in which recirculation occurs in the wake, increasing turbulent mixing and wake diffusion.[5]

Because the wakes of turbines under high thrust coefficients are turbulent, we try to gain an understanding of such wakes by studying the time-averaged flow field. We describe the wake as a vorticity surface that follows a streamline.[28,29] For low thrust coefficients, the vorticity surface starts at the rotor plane and expands as it travels downstream. In the case of high thrust coefficients, the vorticity surface expands near the rotor and then it contracts as it moves downstream. When the radius of the surface is reduced (following the streamlines), the total induction becomes much weaker, reducing the total deficit in the wake. This reduction in wake deficit, combined with the turbulent diffusion, allows for a fast recovery of the wake. All simulations under conditions of high thrust coefficients exhibit the same behavior. This mechanism is consistent across simulations and in all cases with different radial distribution of load. This behavior will be explained using a simplified model.

4.1 | Simplified wake model to better understand wake physics

In this section, we focus on understanding the flow physics through a simplified set of equations. We show a simplified model to compute the velocity field of a wind turbine wake based on a vorticity surface. This model is meant to be used as a way to understand the mechanism of wake evolution and not a detailed description of the flow. The wind turbine wake is represented by a vorticity surface that follows the streamline passing through the circumference of the rotor disk. This approach was used by Øye and van Kuik[28,30] to predict the wake of a wind turbine with thrust coefficients below $C_T = 1$. We extend this model to include cases with higher thrust coefficients and turbulent diffusion. The effect of turbulence diffusion is taken into account by reducing the strength of the vorticity surface as it travels downstream. Figure 11 shows a schematic of the model where the line represents the vorticity surface.

The position of the surface is a streamline of the flow according to Equation (3).

$$R(x) = R_0 + \int_0^x \frac{u_r(x', R(x'))}{u_x(x', R(x'))} dx' \tag{3}$$

Here

- u_x and u_r are the axial and radial velocity induced by the vorticity surface;

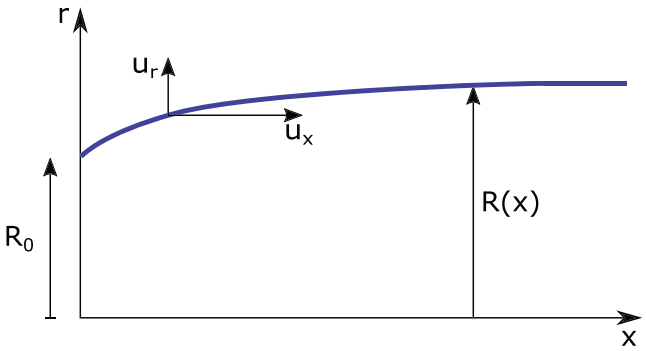

FIGURE 11 Diagram of a streamline used to describe the vorticity surface for the simplified wake model

- R_0 is the radius of the turbine and starting position of the vorticity surface; and
- $R(x)$ is the function defining the location of the surface at every point in space.

Equation (3) is solved numerically by an iterative algorithm to obtain a vorticity surface $R(x)$. The velocity field induced by the vorticity surface is given by the superposition of a collection of infinitesimal vortex rings.[29]

$$u_r(x,r) = \sum_i^N \frac{\Gamma(x_i)k}{4\pi r_0}\frac{x-x_i}{r_0}\left(\frac{r_0}{r}\right)^{\frac{3}{2}}\left[\frac{2-k^2}{2(1-k^2)}E(k^2) - K(k^2)\right] \tag{4}$$

$$u_x(x,r) = \sum_i^N \frac{\Gamma(x_i)k}{4\pi r_0}\left(\frac{r_0}{r}\right)^{\frac{1}{2}}\left[\left(\frac{r_0}{2r}\frac{k^2}{1-k^2} - \frac{2-k^2}{2(1-k^2)}\right)E(k^2) + K(k^2)\right] \tag{5}$$

Here,

$$k^2 = \frac{4rr_0}{(r+r_0)^2 + (x-x_i)^2} \tag{6}$$

and where

- x and r are the streamwise and radial directions;
- x_i is the position of an infinitesimal vortex ring i;
- $\Gamma(x_i)$ is the strength of the vortex ring at location x_i; and
- K and E are the complete elliptic integrals of the 1^{st} and 2^{nd} kind, respectively.

This model is conceptually the same as the one from van Kuik et al. with an added term to include turbulent diffusion.[28] As a first-order approximation, we scale the vorticity as follows:

$$\Gamma(x) = \Gamma(0)\exp\left[-\frac{x\overline{U}_x}{\tilde{\nu}}\right] \tag{7}$$

where $\Gamma(0) = -2a\overline{U}_x dx$, a is the induction at the rotor plane, dx is the infinitesimal vorticity surface width, $\tilde{\nu}$ acts as a turbulent eddy-viscosity, and we adjust it to match the results from LES for each thrust coefficient. For lower thrust coefficients, the turbulence in the wake is small and the eddy viscosity is neglected ($\tilde{\nu} = 0$ when $C_T < 1$). The model uses 300 vortex rings in the current setup and a downstream distance of 8 rotor diameters. The computational time for the code is on the order of seconds on a single CPU.

Figure 12 shows velocity contours with streamlines from the model and LES results using the RPM method to control C_T. The model is able to predict the behavior of the streamlines and the diffusion of the velocity field. The viscosity value used for the high-thrust case ($C_T = 1.3$) was $\tilde{\nu} = 0.3\,\text{m/s}^2$. The diffusion model we introduced leads to a comparable contraction of the vorticity surface compared to the LES results. This mechanism allows for much faster recovery of wind turbine wakes in high-thrust conditions. This model was used to explain the mechanism

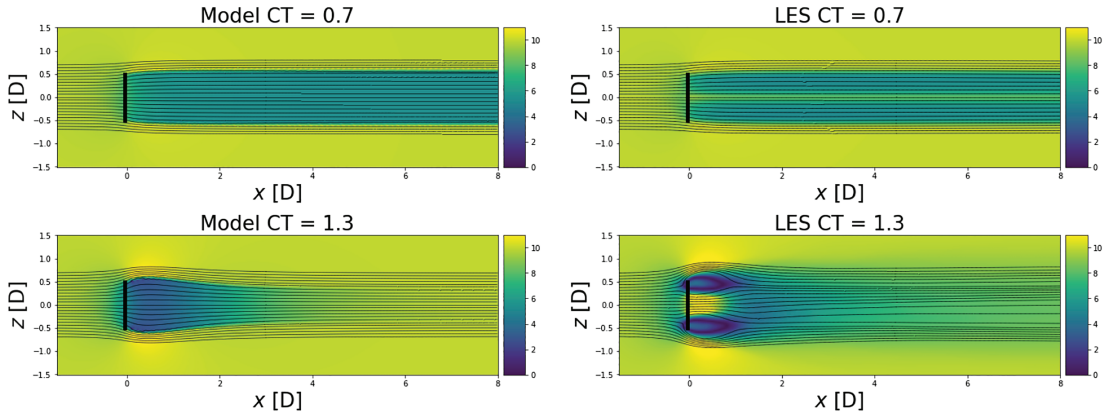

FIGURE 12 Velocity contours and streamlines from the simple model proposed and large-eddy simulations (LES)

behind high-thrust wakes and is not intended to provide an accurate description of the flow in its current form. Further improvements of the model will be considered in the future.

5 | A SIMPLIFIED MODEL FOR FAST.FARM

In this section, we develop an empirical model to predict the wake velocity of a high-thrust wind turbine by fitting the results from LES to a Gaussian profile.[31] We observe that most wake profiles at 3D downstream in high-thrust simulations have reached a fully developed state. These profiles match a Gaussian wake profile.[31] However, the formulations for the standard Gaussian wake model do not apply in the case of high thrust coefficient.[31] This limitation arises because the formulas are only valid for thrust coefficients below $C_T < 24/25$.[1]

FAST.Farm uses a semi-analytical representation of the wake based on blade element momentum theory and the wakes are advected using the inflow velocity field. FAST.Farm solves numerically a simplified form of the axisymmetric Reynolds-averaged Navier–Stokes equations to obtain the velocity deficit.[9,32] To solve the equation numerically, an initial condition of the wake velocity is needed at the rotor plane. In its baseline calculation routine, FAST.Farm initializes the induced velocity of the wake planes as follows:

$$u_{x,\mathrm{LT}}(r_w) = -\overline{U}_x C_{\mathrm{NW}} a(r) \tag{8}$$

where LT stands for 'low thrust', r and r_w are the radius along a same streamline at the rotor and the wake respectively, $\overline{U}_x$ is the time-filtered rotor-disk-averaged relative wind speed, C_{NW} is a tuning constant for the near wake (with a default value of $C_{\mathrm{NW}} = 1.8$), and $a(r)$ is the radially dependent induction, which is derived from the radially dependent local thrust coefficient using momentum theory. In practice, momentum theory and the conservation of mass are used to relate the two radii, considering wake expansion in the near wake, and the wake planes are initialized at the rotor plane. More details on the baseline implementation are given in the FAST.Farm User's Guide and Theory Manual.[33] The relationship between the radii becomes invalid when the local thrust coefficient (C_t) exceeds 24/25. In this work, we revised this calculation routine such that the local thrust coefficient used in the wake calculation is capped at a maximum value of 24/25. The relationship between r and r_w can then be computed, even when the rotor is highly loaded, and Equation (8) can be evaluated. We nevertheless expect that the accuracy of this formula will decrease as the loading increases, therefore we will suggest another model for this regime.

Following the observations of the Gaussian wake for high thrust coefficients, we propose the following fit for the far wake for turbines with a high thrust coefficient:

$$u(r)_{\mathrm{HT}} = -\mu \overline{U}_x \exp\left(-r^2/(D^2\sigma^2)\right), \tag{9}$$

where HT stands for "high thrust," and D is the rotor diameter. In this model, no distinction is necessary between r_w and r.[31] The Gaussian parameters μ and σ were determined by fitting a Gaussian shape that best matches the wake velocity profiles obtained for each simulation in the far wake between 4–6 diameters downstream. The coefficients were then adjusted to be valid near the rotor, since FAST.Farm emits a fully developed wake at the rotor. The tuned Gaussian coefficients are as follows:

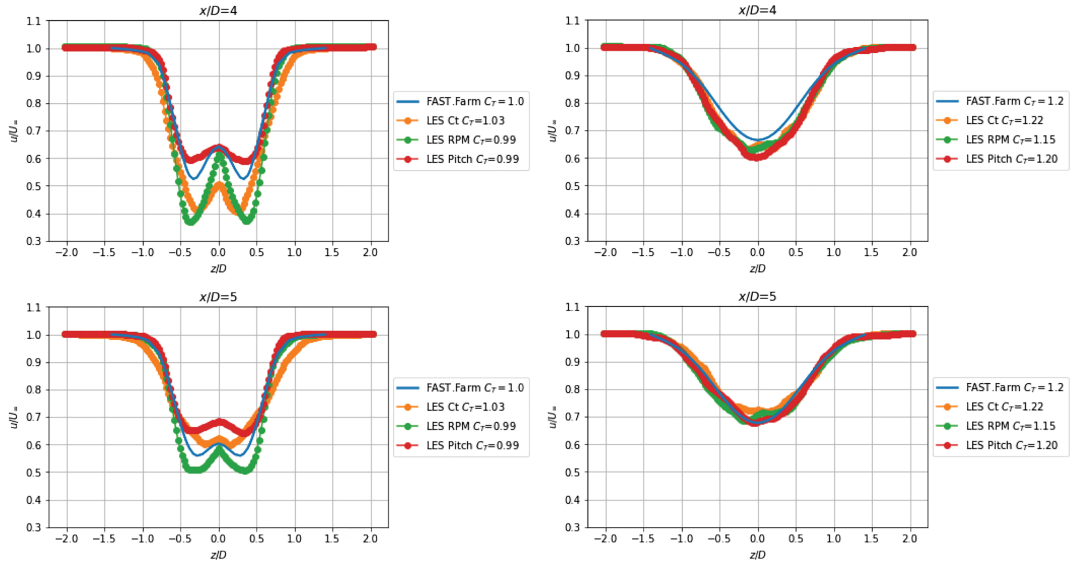

FIGURE 13 Wake velocity at 4*D* (top) and 5*D* (bottom) downstream with nominal thrust coefficients of $C_T = 1$ (left) and $C_T = 1.2$ (right)

$$\mu(C_T) = \frac{0.3}{2C_T^2 - 1} + \frac{1}{5}, \quad \sigma(C_T) = \frac{C_T}{2} + \frac{4}{25} \tag{10}$$

We now propose an engineering model to blend the two approaches given in Equations (8) and (9) in the region where the accuracy of both model starts to decrease. We define the blending coefficient, α, which varies linearly from 1 to 0 between $C_T = 24/25$ and $C_T = 1.2$. In the blending region, the velocity deficit is given as follows:

$$u_x = \alpha u_{x,\mathrm{LT}} + (1 - \alpha) u_{x,\mathrm{HT}} \tag{11}$$

Before and after the blending region, the LT and HT formulae are used, respectively. FAST.Farm uses the rotor disk averaged thrust coefficient (without capping of the local thrust coefficient) when computing α and C_T in Equation (10). The Gaussian parameters of the HT model are computed using Equation (10).

We performed simulations using the new model in FAST.Farm and compared it to the LES results. Figure 13 shows the wakes (4*D* and 5*D*) of FAST.Farm compared to LES results for thrust coefficients of $C_T = 1$ and $C_T = 1.2$. The time averaged thrust coefficient from each case is shown in the figure legend. We can see agreement between FAST.Farm and the LES for the downstream distances presented. This model depends only on the mean thrust coefficient and not on blade load distribution when computing the high thrust formulas. Possible improvements of the model could be achieved by taking into account the blade loading.

This model proposed for FAST.Farm is a simplified version of wind turbine wakes at high thrust coefficients. This model resolves previous inconsistencies that would make FAST.Farm abort when reaching high thrust coefficients.[9,33] We have noticed that the turbulence levels in the wake reach high values (above 20%–30%), which is higher than most atmospheric conditions when using FAST.Farm (and not captured in this simplified model). The levels of turbulence in the wake are much higher than the turbulence levels in the atmosphere, which suggests that the wake behavior is dominated by the high-thrust wake physics. Future work will focus on studying wind turbine wakes with high thrust coefficients under turbulent inflow.

6 | CONCLUSIONS

In this work, we studied wind turbine wakes under high-thrust conditions using LES. The inductions at the rotor for low-thrust conditions matches axial momentum theory closely. For higher thrust coefficients ($C_T > = 24/25$), the relationship between thrust coefficient and axial induction is scattered and does not follow a clear trend, agreeing with previous findings in the literature. Wind turbine wakes in high-thrust conditions are different when compared to the standard wind turbine wakes ($C_T < = 24/25$). The main difference was observed from the time-averaged streamlines. In the case of low-thrust wind turbine wakes, the streamlines expand as they pass through the rotor and keep expanding until local pressure

recovers to freestream pressure, at which point the streamlines stop expanding. In the case of high thrust coefficients, the streamlines expand near the rotor and then contract. This contraction allows for faster recovery of the wake.

A simple model of a vorticity surface was adapted to predict the time-averaged velocity field of a wind turbine under high-thrust conditions. The main trends of the LES were captured by the model by using an eddy viscosity term to represent the effects of turbulent diffusion. This allowed for the streamlines to expand near the rotor and then contract as the wake evolves downstream. The turbulent diffusion combined with the wake contraction enhance wake recovery. Based on fitting the LES results, we also developed an empirical model to predict the near-wake of wind turbine wakes with high thrust coefficients. These wakes for high-thrust conditions are described by a Gaussian profile. The simple fit is now implemented inside the near-wake correction model of FAST.Farm and preliminary tests show that this implementation resolves prior issues where FAST.Farm would otherwise abort.

Some possible improvements for the FAST.Farm model would be to (1) add a near wake model for high-thrust conditions; (2) include atmospheric turbulence in the Gaussian model; (3) add a model that depends on the blade load distribution; (4) change the eddy viscosity model so that the wake recovers downstream quickly under high-thrust conditions; and (5) handle wake-added turbulence under high-thrust conditions. These improvements will be a part of future work. We note that the wakes generated by turbines operating in high-thrust conditions experience an enhanced recovery mechanism. Further investigation of this mechanism will be considered as part of future work for wake mitigation strategies. Future work should also focus on studying wakes of wind turbines at high thrust coefficients with finite number of blades, such as actuator line and blade resolved simulations.

ACKNOWLEDGEMENTS

A portion of the research was performed using computational resources sponsored by the US Department of Energy's Office of Energy Efficiency and Renewable Energy and located at the National Renewable Energy Laboratory. This work was authored in part by the National Renewable Energy Laboratory, operated by Alliance for Sustainable Energy, LLC, for the US Department of Energy (DOE) under Contract No. DE-AC36-08GO28308. Funding provided by the US Department of Energy Office of Energy Efficiency and Renewable Energy Wind Energy Technologies Office. The views expressed in the article do not necessarily represent the views of the DOE or the US Government. The US Government retains and the publisher, by accepting the article for publication, acknowledges that the US Government retains a non-exclusive, paid-up, irrevocable, worldwide license to publish or reproduce the published form of this work, or allow others to do so, for US Government purposes.

Sandia National Laboratories is a multimission laboratory managed and operated by National Technology & Engineering Solutions of Sandia, LLC, a wholly owned subsidiary of Honeywell International Inc., for the US Department of Energy's National Nuclear Security Administration under contract DE-NA0003525.

PEER REVIEW

The peer review history for this article is available at https://publons.com/publon/10.1002/we.2688.

DATA AVAILABILITY STATEMENT

The data that support the findings of this study are available from the corresponding author upon reasonable request.

ORCID

Luis A Martínez-Tossas https://orcid.org/0000-0003-2353-4999
Kelsey Shaler https://orcid.org/0000-0002-7563-3377

REFERENCES

1. Moriarty PJ, Hansen AC. Aerodyn theory manual. tech. rep., Golden, CO (US), National Renewable Energy Lab.; 2005.
2. van der Tempel J, Molenaar D-P. Wind turbine structural dynamics—a review of the principles for modern power generation, onshore and offshore. *Wind Eng*. 2002;26(4):211-222.
3. Madsen HA, Larsen GC, Larsen TJ, Troldborg N, Mikkelsen R. Calibration and validation of the dynamic wake meandering model for implementation in an aeroelastic code. *J Solar Energy Eng*. 2010;132(4):41014. https://doi.org/10.1115/1.4002555
4. Johnson W. *Helicopter theory*, *Second edition*, Dover books on physics. Dover Publications, Mineola, N.Y.; 1994.
5. Eggleston DM, Stoddard FS. *Wind turbine engineering design*. Van Nostrand Reinhold; 1987.
6. Glauert H. *Airplane Propellers*, *Division L*. W.F. Durand (ed), Vol. 4. Julius Springer, Berlin; 1935.
7. Buhl Jr ML. New empirical relationship between thrust coefficient and induction factor for the turbulent windmill state. tech. rep., Golden, CO (United States), National Renewable Energy Lab.; 2005.
8. Jonkman J, Doubrawa P, Hamilton N, Annoni J, Fleming P. Validation of fast. Farm against large-eddy simulations. *J Phys Conf Ser*. 2018;1037(6):62005.
9. Shaler K, Jonkman J. Fast.farm development and validation of structural load prediction against large eddy simulations. *Wind Energy*. 2020;24(5):428-449. https://onlinelibrary.wiley.com/doi/abs/10.1002/we.2581

10. Sprague MA, Ananthan S, Vijayakumar G, Robinson M. Exawind: A multifidelity modeling and simulation environment for wind energy. In: Nawea/Windtech 2019 Conference IOP Publishing; 2019; Amherst, MA.
11. Domino SP. Toward verification of formal time accuracy for a family of approximate projection methods using the method of manufactured solutions. *Proc 2006 Summer Prog Center Turbulence Res*. 2006;11:163-177.
12. Domino SP. A comparison of various equal-order interpolation methodologies using the method of manufactured solutions. *Proc 2008 Summer Progr Center Turbulence Res*. 2008:97-111.
13. Domino SP. A comparison between low-order and higher-order low-mach discretization approaches. In: Proceedings of the Summer Program Center for Turbulence Research; 2014:387.
14. Domino SP, Sakievich P, Barone M. An assessment of atypical mesh topologies for low-mach large-eddy simulation. *Comput Fluids*. 2019;179:655-669.
15. Maniaci DC, Moriarty PJ, Barone MF, Churchfield MJ, Sprague MA, Arunajatesan S. Wind energy high-fidelity model verification and validation roadmap. tech. rep., Albuquerque, NM (US), Sandia National Lab.; 2020. https://www.osti.gov/biblio/1634281
16. Blaylock ML, Houchens BC, Maniaci DC, et al. Comparison of field measurements and large eddy simulations of the scaled wind farm technology (swift) site. In: ASME-JSME-KSME 2019 8th Joint Fluids Engineering Conference American Society of Mechanical Engineers Digital Collection; 2019.
17. Doubrawa P, Quon EW, Martinez-Tossas LA, et al. Multimodel validation of single wakes in neutral and stratified atmospheric conditions. *Wind Energy*. 2020;23(11):2027-2055. https://onlinelibrary.wiley.com/doi/abs/10.1002/we.2543
18. Sakievich P, Knaus RC, Hsieh A, et al. A2e high-fidelity modeling (HFM) project overview of fy20 q2 milestone completion: actuator disk improvements and hardening. SAND2020-3817PE, Livermore, CA (United States), Sandia National Lab.; 2020. https://www.osti.gov/biblio/1774749
19. Hsieh A, Maniaci DC, Herges TG et al. Multilevel uncertainty quantification using cfd and openfast simulations of the swift facility. In: AIAA SCITECH 2020 FORUM AIAA Scitech; 2020:1949. https://arc.aiaa.org/doi/abs/10.2514/6.2020-1949
20. Sørensen JN, Shen WZ. Numerical modeling of wind turbine wakes. *J Fluids Eng*. 2002;124(2):393-399.
21. Troldborg N. Actuator line modeling of wind turbine wakes. *Ph.D. Thesis*: Danish Technical University, Lyngby, Denmark; 2009.
22. Martínez-Tossas LA, Churchfield MJ, Leonardi S. Large eddy simulations of the flow past wind turbines: actuator line and disk modeling. *Wind Energy*. 2015;18(6):1047-1060.
23. Smagorinsky J. General circulation experiments with the primitive equations: I. The basic experiment*. *Monthly Weather Rev*. 1963;91(3):99-164. https://doi.org/10.1175/1520-0493(1963)091<0099:GCEWTP>2.3.CO;2
24. Martínez-Tossas LA, Churchfield MJ, Yilmaz AE, et al. Comparison of four large-eddy simulation research codes and effects of model coefficient and inflow turbulence in actuator-line-based wind turbine modeling. *J Renew Sustain Energy*. 2018;10(3):33301.
25. Jonkman J, Butterfield S, Musial W, Scott G. Definition of a 5-mw reference wind turbine for offshore system development. tech. rep., Golden, CO (United States), National Renewable Energy Lab.; 2009.
26. Madsen HA, Larsen TJ, Pirrung GR, Li A, Zahle F. Implementation of the blade element momentum model on a polar grid and its aeroelastic load impact. *Wind Energy Sci*. 2020;5(1):1-27. https://wes.copernicus.org/articles/5/1/2020/
27. Madsen HA. A CFD analysis of the actuator disc flow compared with momentum theory results. In: Proc. 10th IEA Symp. on the Aerodynamics of Wind Turbines IEA Symp.; 1996; Edinburgh:109-124.
28. Van Kuik GAM, Lignarolo LEM. Potential flow solutions for energy extracting actuator disc flows. *Wind Energy*. 2016;19(8):1391-1406.
29. Branlard E. *Wind turbine aerodynamics and vorticity-based methods: Fundamentals and recent applications*. Springer International Publishing; 2017.
30. Øye S. A simple vortex model of a turbine rotor. In: Proc. of the Third IEA Symposium on the Aerodynamics of Wind Turbines Danish Technical University; 1990; Etsu, Harwell:4.1-1.15.
31. Bastankhah M, Porte-Agel F. A new analytical model for wind-turbine wakes. *Renew Energy*. 2014;70:116-123. Special issue on aerodynamics of offshore wind energy systems and wakes.
32. Ainslie JF. Calculating the flowfield in the wake of wind turbines. *J Wind Eng Indust Aerodyn*. 1988;27(1):213-224. http://www.sciencedirect.com/science/article/pii/0167610588900372
33. Jonkman J, Shaler K. Fast.farm user's guide and theory manual. tech. rep., Golden, CO (US), National Renewable Energy Lab.; 2020.

How to cite this article: Martínez-Tossas LA, Branlard E, Shaler K, et al. Numerical investigation of wind turbine wakes under high thrust coefficient. *Wind Energy*. 2022;25(4):605-617. doi:10.1002/we.2688